Spatially Addressable Multiplex Biodetection by Calibrated Micro/Nanostructured Surfaces

Serban Dobroiu,[#] Falco C.M.J.M. van Delft,[#] Ayyappasamy Sudalaiyadum Perumal,[#] Shantoshini Dash, Jenny Aveyard, Jeroen van Zijl, Jaap Snijder, Eric van den Heuvel, Jurgen van Berkum, Marie Pierre Blanchard, Cyril Favard,* and Dan V. Nicolau*
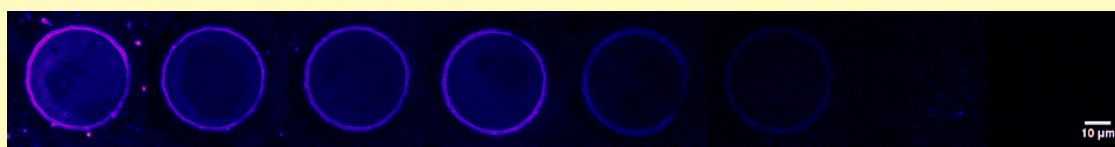
Read Online

ACCESS | Metrics & More | Article Recommendations | Supporting Information

ABSTRACT: A challenge of any biosensing technology is the detection of very low concentrations of analytes. The fluorescence interference contrast (FLIC) technique improves the fluorescence-based sensitivity by selectively amplifying, or suppressing, the emission of a fluorophore-labeled biomolecule immobilized on a transparent layer placed on top of a mirror basal surface. The standing wave of the reflected emission light means that the height of the transparent layer operates as a surface-embedded optical filter for the fluorescence signal. FLIC extreme sensitivity to wavelength is also its main problem: small, e.g., 10 nm range, variations of the vertical position of the fluorophore can translate in unwanted suppression of the detection signal. Herein, we introduce the concept of quasi-circular lenticular microstructured domes operating as continuous-mode optical filters, generating fluorescent concentric rings, with diameters determined by the wavelengths of the fluorescence light, in turn modulated by FLIC. The critical component of the lenticular structures was the shallow sloping side wall, which allowed the simultaneous separation of fluorescent patterns for virtually any fluorophore wavelength. Purposefully designed microstructures with either stepwise or continuous-slope dome geometries were fabricated to modulate the intensity and the lateral position of a fluorescence signal. The simulation of FLIC effects induced by the lenticular microstructures was confirmed by the measurement of the fluorescence profile for three fluorescent dyes, as well as high-resolution fluorescence scanning using stimulated emission depletion (STED) microscopy. The high sensitivity of the spatially addressable FLIC technology was further validated on a diagnostically important target, i.e., the receptor-binding domain (RBD) of the SARS-Cov2 via the detection of RBD:anti-S1-antibody.

KEYWORDS: microarrays, diagnostic devices, microstructures, nanostructures, fluorescence interference contrast

The simplicity of 2D microdevices for diagnostics, e.g., ELISA assays, and for high-throughput screening, e.g., microarrays, made them widely used. For instance, despite the success of various 3D devices for New Generation Sequencing, planar microarrays are still used for much of the genomics[1−3] and for almost all proteomics work.[4] Likewise, fluorescence is still the chosen method for detection of biomolecular recognition despite its drawbacks, e.g., signal nonlinearity at high fluorophore concentrations,[5] variation of the signal intensity, emission wavelength modulated by molecular environment,[6] and time variation of the signal due to photobleaching.[7]

One line of research regarding the performance of planar devices for diagnostics and high-throughput screening aims to improve the characteristics of the fluorescence signal, e.g., its intensity, signal/noise ratio, and image contrast, by using micro- and nanostructures on the device surface. First, micro- and nanostructures can increase the rate and level of biomolecular recognition events via increased exposure to surface-immobilized probes and thus increase the fluorescence

signal, e.g., by using micron and submicron sized pillars,[8,9] wires,[10,11] polymeric microstructures,[12−14] or beads.[15,16] A second benefit of microstructuring is the improved quantification of the fluorescence signal facilitated by precisely patterned regions of interest, via, e.g., polymer lift-off arrays,[17,14] bar-coded lines,[12,13] or dots.[15,16] The third and arguably the most fundamental benefit offered by micro/nanostructuring rests on the modulation of the fluorescence signal by transparent layers, e.g., silicon dioxide (SiO_2), with calibrated heights, via the fluorescence interference contrast (FLIC) phenomenon, whose theory is well documented[18−20] and which was used in microarray technology.[21−24] However,
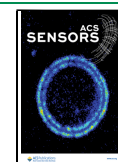
the implementation of FLIC technology is not without problems. For instance, complex multilayered surfaces[21−23] will optimize the signal for all fluorescence wavelengths at the cost of not being able to fully optimize it for a particular one. Conversely, various patterned micro/nanostructures, each optimized for a particular fluorophore, can be placed on various regions of the device surface, thus spatially encoding the fluorescence signal. However, this type of fabrication requires more microlithographic steps, consequently increasing the cost. Importantly, the height of FLIC structures is precisely optimized for a nominal fluorophore, making them unable to accommodate inherent variations of a fluorescence signal, due to the actual vertical position of the fluorophore on the surface-immobilized biomolecules, which can have sizes comparable with the quarter of fluorescence wavelength, thus offsetting the FLIC effect.

To this end, the present contribution reports on the lateral and vertical micro- and nanostructuring, respectively, of surfaces leading to improvement of fluorescence signal characteristics and thus to increased sensitivity and reliability of microarrays.

■ MATERIALS AND METHODS

Substrate Fabrication. Variable height and footprint micro-terraces were patterned on predeposition Ar^+ sputter-cleaned silicon wafers. A 100 nm thick Pt layer was sputter deposited, if needed, preceded by a 10 nm thick Ti adhesion layer. Subsequently, SiO_2 layers with thicknesses of 20, 40, 60, 80, and 100 nm, respectively, were deposited onto all the wafers. All sputter deposition processes were carried out using a Veeco Nexus 800 sputter deposition tool (process parameters detailed elsewhere[16,24,25]). Next, a 1.5 μm thick HPR504 resist layer was spin coated on the wafers, soft-baked at 95 °C for 2 min, exposed on an ASML i-line stepper using a standard "lines and spaces" test reticule, and developed for 2 min at 21 °C in Tetramethylammonium hydroxide (TMAOH). The structured resist was used as an etch mask to transfer the pattern to the SiO_2 layer using a CHF_3 plasma (with a 10% overetch), followed by a short high-pressure O_2/N_2 plasma treatment, to remove fluorinated deposits resulting from the CHF_3 (trifluoromethane)reactive ion etching (RIE) step, and wet-chemical resist removal.

A second set of FLIC geometries consisted of lenticular structures, which were fabricated on 6 in. wafers using a similar technology. To obtain the sloping walls, the RIE process parameters were continuously fine-tuned to ensure a deliberate low etch selectivity (SiO_2/resist) with considerable mask width loss. The height of these structures was 400 nm with various diameters and pitches. The measured mean slope of the walls was 12°. The etching was stopped when ∼60 nm of SiO_2 thickness remained outside the mask protected area. After mask removal and a first round of fluorescence experiments, the wafers were etched again (this time without a mask) to remove ∼60 nm of SiO_2 thickness everywhere on the wafer.

Surface Functionalization. (3-Aminopropyl) triethoxy-silane (APTES) was purchased from Sigma-Aldrich. Amine-reactive DyLight 488, 550, and 650, respectively, were purchased from Thermo Scientific. PBS, 15 mM sodium phosphate, 0.15 M NaCl, pH 7.4, bicarbonate buffer, 0.1 M sodium bicarbonate, pH 8.2, bicarbonate buffer 0.1 M, sodium bicarbonate containing 10% ethanol, and PBS containing 0.05% tween20 were made with analytical grade reagents. Prior to silanization, a dry photochemical cleaning procedure was applied to the substrates using a Bioforce Nano UV-ozone chamber. Amino-silanization was carried out on a rocker plate mixer in an ethanol/4.25 M acetic acid/APTES (95:3:2) mixture at room temperature for 2 h followed by four ethanol washes and curing at 110 °C for 45 min. For NHS-derivatized probe attachment, the aminosilanized substrates were slow-tilt rotated at room temperature for 4 h with 10 μM NHS ester dye in bicarbonate buffer. Unbound

dye was removed by one wash in bicarbonate wash buffer and three washes in the PBS wash buffer, while nitrogen was used for drying.

Surface Characterization. Time-of-flight secondary ion mass spectrometry (TOF-SIMS) measurements were performed using an Ion-ToF IV instrument, using 25 keV Bi+ primary ions, in both positive and negative mode. The mass resolution $\Delta M/M$ is larger than 6000 for masses above ∼20. The surface topography of lenticular structures was measured using a Veeco CP-II AFM in tapping mode by measuring both the cantilever oscillation amplitude and the error signal. SPM image processing was performed using the WSxM[26] software package (Nanotec Electronica, Madrid, Spain).

Imaging. Fluorescence images for initial characterization were obtained with a Zeiss Observer microscope equipped with an LSM 510 laser scanning confocal module using appropriate laser lines and filters (imaging parameters are available in the Supporting Information). The images, in their original format, were processed using the ImageJ package[27] together with the LSM Reader, LSM Toolbox, and Radial profile plug-ins. The fluorescence assay with COVID-19 antigen recognition was performed using an Olympus IX53 microscope, with UPlanSApo 20X/0.75 air objective (Olympus, Japan). Stimulated emission depletion (STED) microscopy was performed using a STED microscope (Expert Line, Abberior Instruments, Germany) equipped with a PlanSuperApo 100X/1.40 oil immersion objective (Olympus, Japan) and a 775 nm depletion laser line. Images were obtained at 561 nm excitation. The dwell time was set to 10 μs, and images were collected in line accumulation mode (12 lines). Fluorescence was detected using avalanche photodiodes and spectral detection (600−700 nm). The pinhole was set to 1.0 Airy units, and a pixel size of 30 nm was used for all acquisitions (see details in the Supporting Information).

Optical Simulation. Optical models were obtained using a custom routine written either for MatLab or for the freely available software Freemat.[28] Data processing, fitting, and graph making were done using Origin Lab (Origin Lab, Northampton, MA, USA). A complete description of the modeling is presented in the Supporting Information.

Biomolecular Recognition of the RBD of SARS-Cov-2. The receptor binding domain (RBD) of SARS-Cov2, used in this study, was produced by transient transfection in HEK-293SF (serum-free) suspension cells using a construct described previously[29] in HyCellTransFX-H media supplemented with 0.1% kolliphor and 6 mM Glutamax. The 38 kDa RBD antigen secreted in the culture supernatant was concentrated up to four times through Amicon Ultra centrifugal filters-10K (Millipore). The anti-S1 antibody recognizes the N-terminal of the S1 subunit of spike glycoprotein of SARS-CoV-2. Surface functionalization was carried out using APTES-silanization similar to the protocol detailed above. The unlabeled purified RBD was first surface-functionalized onto the FLIC substrate (30 min), followed by repeated washing (three times) with 1X PBS, and then subsequently hybridized with AF594-labeled anti-S1 mouse IgG antibody (30 min, final hybridizing concentration 1 ng/μL). An amount of 1 μL of anti-S1 antimouse IgG antibody (1 mg/mL) was labeled with AlexaFluor 594 (AF594) in a total final reaction volume of 100 μL of 1X PBS using the ZenonTM Mouse IgG1 labeling kit (Catalog number: Z25007). The hybridized substrates were washed repeatedly (at least three times) with 1X PBS, dried in a N_2 chamber, and imaged as described above. The above biorecognition approach was adopted for plotting the limit of detection (LoD) graphs with different concentrations starting from 10 ng/μL up to 0.00001 ng/μL of the RBD-S1 SARS-CoV-2 antigen bound on the surface.

■ RESULTS AND DISCUSSION

Theoretical Framework. FLIC, which refers to the modulation of fluorescence by the distance between the fluorophore and a reflecting surface and the subsequent formation of standing waves, was described previously,[18] with a comprehensive mathematical description also available.[20] In this work, the separation distance between the fluorophore and the reflector was provided by SiO_2 layers. The interference

between the direct and reflected light, for both excitation and emission, gives rise to standing waves characterized by intensity maxima and minima along the vertical axis rising from the reflecting surface. When the vertical position of the fluorophore on top of the SiO_2 structures coincides with these maxima or minima, fluorescence amplification or suppression, respectively, takes place.

The FLIC theoretical formalism of this 1D model can be used to construct an optical setup, where the fluorophore-to-reflector distance leads to maximum constructive interference and consequently maximum fluorescence enhancement, using a proportional mathematical relationship between the fluorophore excitation and emission wavelengths, respectively, its distance from the reflector, the effective optical path length, and the reflection coefficients of the reflector for a particular fluorophore, as described by eq 1::

$$F_{exp} \propto \left[(1 - r_{ex})^2 + 4 r_{ex} \sin^2\left(\frac{2\pi}{\lambda_{ex}} nd\right) \right] \left[(1 - r_{em})^2 + 4 r_{em} \right.$$
$$\left. \sin^2\left(\frac{2\pi}{\lambda_{em}} nd\right) \right] \tag{1}$$

where r_{ex} and r_{em} are the reflectance coefficients at the excitation and emission wavelengths, respectively; λ_{ex} and λ_{em} are the excitation and emission wavelengths, respectively; n is the refractive index of the medium traversed by light; d is the fluorophore−reflector separation distance; and F_{exp} is the experimentally observed fluorescence intensity (in arbitrary units).where r_{ex} and r_{em} are the reflectance coefficients at the excitation and emission wavelengths, respectively; λ_{ex} and λ_{em} are the excitation and emission wavelengths, respectively; n is the refractive index of the medium traversed by light; d is the fluorophore−reflector separation distance; and F_{exp} is the experimentally observed fluorescence intensity (in arbitrary units). The reflection at the air−SiO_2 interface was ignored, as being typically less than 4%.[30]

For example, when exciting a DyLight650 probe placed on SiO_2 (refractive index of 1.456) at 633 nm and recording its emission at 670 nm and using the reflection coefficients either at the SiO_2−Si or the SiO_2−platinum (Pt) interfaces, respectively (calculated using Fresnel's equations[31−33]), the optimum fluorophore-to-reflector distance was found to be approximately 110 nm.

Microterraces. The modulation of the fluorescence signal by the geometric and material properties of the surface was calibrated using "combinatorial" experiments comprising the recording and analysis of fluorescence on microterraces, with various vertical and lateral dimensions. The microstructures comprise (i) a reflector surface, i.e., Si, or Pt; (ii) a transparent SiO_2 spacer between the fluorophore and the mirror; and, where applicable, (iii) an intermediate titanium dioxide adhesion layer between the SiO_2 and Pt surfaces. Figure 1 shows the fluorescence modulation (in false color) by the height of microterraces (on a Pt reflector) with heights of 40, 60, 80, and 100 nm, respectively (a flat surface is included as control).

Microterraces with heights of 20, 40, 60, 80, and 100 nm were used to validate and extract the parameters for eq 1 (the fit of the theoretical 1D model on fluorescence values measured on a flat surface and microterraces with the heights of the microterraces is detailed in the Supporting Information). The modulation of the fluorescence intensity by the height of
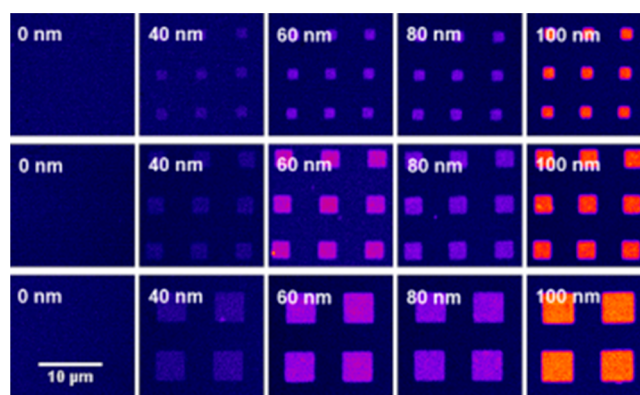

Figure 1. Fluorescence modulation (in false color) by the height of microterraces.

the structures is illustrated in Figure 1. The intensity is modulated by the microterrace height, as generally predicted by eq 1. The diagram showing a simplified optical setup valid for the substrates presented in this paper is shown in Figure S1. For the microterraces with identical heights, a brighter fluorescence was observed on structures having a larger footprint (in Figure S2, for 25 μm^2 versus 9 μm^2 and 4 μm^2 microterraces, respectively), as also reported before.[24] Figure S2 also provides intensity results for much smaller areas, namely, 1 μm^2, 1.56 μm^2, and 2.25 μm^2 areas for the terraces. The use of FLIC was also reported before,[14] where CVD deposited polymeric steps, resulting in the amplification of the fluorescence signal in the region of interest and its quenching outside. However, the variation of the fluorescence signal close to the microterrace walls was not apparent because the reported structures had larger footprints, i.e., above 100 μm.

The likely cause of this variation can be assigned to the departure from the ideal, laterally infinite layers, as assumed by the 1D model in eq 1. First, the fluorescence on the vertical walls can experience both amplification and quenching for the fluorophores placed at different heights, with all these signals overlapping vertically in a difficult to predict manner. Second, the light emitted by the fluorophores can interact in a complex fashion with the lateral walls of the microterraces, e.g., by refraction and reflections, resulting in a loss of intensity. Third, it is noteworthy to observe the light frame around each microterrace, which had different intensities for each footprint size. In addition to the possible explanations presented above, this feature can be the result of the loss of photolithographic resolution at smaller feature sizes resulting in nonvertical and uneven walls. Alternatively, as the microterrace footprint increases, the fraction of the edge pixels in the total number of pixels becomes smaller, and the information contained in the edge pixels can be "contaminated" from the background information on the surrounding pixels.

This uneven lateral distribution of fluorescence and its complex relationship with the size of the footprint of the microterraces (presented in more detail in the Supporting Information and the Supporting Information reported previously[24]) led to the quantification of fluorescence signal dependent on the size of the spot. Also, the lack of flexibility in accounting for the actual vertical position of the fluorophores suggested that a different FLIC geometry needed to be used. Consequently, microterraces, which were also reported before,[24] were used only to calibrate the design of the

lenticular structures and for the comparison of their respective performance characteristics.

Continuous Slope and Lenticular Domes for Multicolor Multiplex Arrays. Substrates using optical coatings that enhance fluorescence signal were reported for protein arrays[25,34] and for DNA arrays.[22,35] The operational principle is that a dielectric stack of layers can be designed to act as a reflector across a range of wavelengths by choosing the optimal materials, their thickness, and the sequence of their stacking. Thus, the fluorescence that would be otherwise lost through the substrate is recovered and reflected toward the detector. Moreover, due to the direct and reflected light interference, the composition of the stack can be designed so that this interference yields a theoretical enhancement factor of 4.[21] The fabrication of such a stack is complex since it comprises at least 10 layers, but it was shown that similar results can be obtained using a simple SiO_2 layer if the proper reflector is placed underneath it.[36,37] While this represents important progress, the common feature of these optical coatings is that their fluorescence enhancement capabilities are optimized for a relatively narrow band in the visible spectrum, for instance, defined by the Cy3/Cy5 pair of fluorophores, which is the standard for bicolor microarrays. Moreover, there is an innate limitation of these devices in that the spectral width over which one can obtain high reflectivity is limited by the refractive index contrast between the materials used. This limitation is fundamental, as the bandwidth depends on the disparity between the refractive index values.[38] For instance, for an optical stack comprising MgF_2 and TiO_2 and for a central wavelength of 633 nm, a bandwidth of less than 250 nm is expected. Of course, devices displaying wide band characteristics are available, e.g., in the form of chirped reflectors,[39] but at the expense of a higher system complexity.

A possible geometry allowing FLIC to manifest irrespective of the emission wavelength of the fluorophore consists of optically transparent structures with continuous sloping side walls, rather than step terraces. Such a lenticular structure is presented in Figure 2. While the dimensions of these structures can be arbitrarily chosen, the quasi-lenticular structures used here have very flat trapezoidal transversal profiles, with heights of 420 nm and diameters of 40 μm and an average slope of approximately 12°. Also visible in the reflected light micrograph is the dark and bright ring structure due to light interference.

The hypothesis that structures like those presented in Figure 2 can be used to enhance the emission of various fluorophores was first tested by conjugating DyLight 650 on top of lenticular microstructures in two variants. Figure 3 shows the two surfaces with (A) no SiO_2 layer in the unmasked area and with (B) a bottom 60 nm SiO_2 layer and the respective AFM height profiles (C, D). Figure 3 (E−G) shows the comparison of typical fluorescence micrographs of 40 μm wide lenticular structures after surface conjugation of DyLight 650, respectively, without (E) and with (F) the residual 60 nm thick SiO_2 layer. The fluorescence image of lenticular structures with no SiO_2 layer on the Pt reflecting surface in the unmasked area (Pt functionalized with a different chemistry than the SiO_2 surface) presents normal red fluorescence on the flat part of the structure but also typical interference contrast rings on the lateral slopes (Figure 3E). Conversely, if a SiO_2 layer (60 nm) is present at the base of the lenticular structures and on top of the Pt reflector, the fluorescence image is reversed (F): the flat top of the lenticular
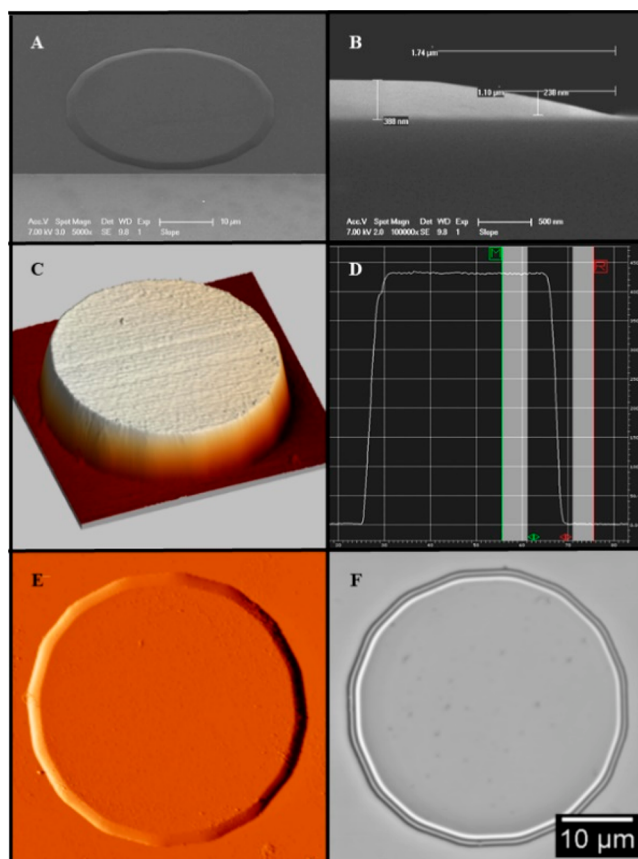

Figure 2. Geometry of the lenticular microstructures. SEM micrographs: (A) top view and (B) side view. AFM scanned images: (C) 3D view and (D) measurement of heights and profiles. Optical microscopy images: (E) DIC image and (F) reflected light optical image (note the optical interference). Scale bar shown in F is also valid for microscopy images in C and E.

structure experiences quenching of fluorescence at 385 nm height, whereas the areas of the structure present regular red fluorescence at 60 nm height. Figure 3 also presents a quantified position of the DyLight 650 fluorescent rings (G), which correlates well, albeit not perfectly, with the 1D prediction of the position of the maxima and minima of fluorescence intensity (H). The effect of optical slicing on contrast and the respective micrographs are presented in SI-5 and Figure S3.

As the multiplexing capability is to a large extent controlled by the capacity of resolving fluorescent patterns, we explored the limits of resolving FLIC patterns on much smaller domes, i.e., 10 μm in diameter (as opposed to 40 μm), using stimulated emission depletion (STED) microscopy,[40] which can resolve images down to 100 nm. While STED is not appropriate for diagnostic applications, as it is based on deactivation of fluorophores, even if selective, the method can be used for super-resolution imaging.[40,41] Using STED microscopy, not only were the separations between FLIC features clearly visible (Figure 4A and the inset) but also the relative intensity of the respective fluorescence signals could be quantified (Figure 4B−D). Furthermore, in Figure 4D, the peak separation of the rings can be observed at 700 nm apart rings and the elevation of the rings around 410 and 440 nm. The experimental values shown here were found to be in
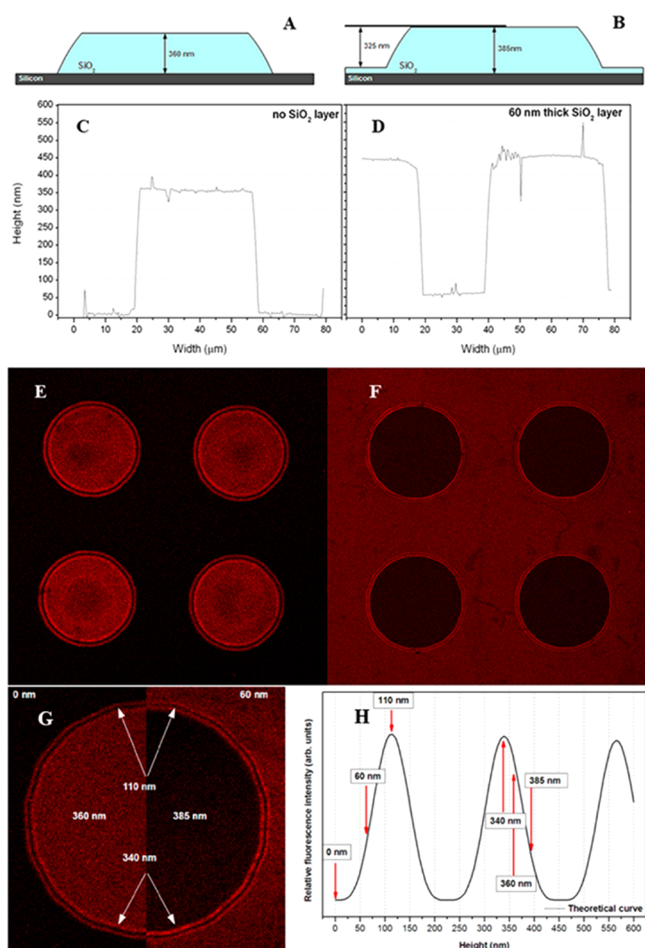
Figure 3. Design and AFM characterization of two different SiO$_2$-coated lenticular microstructures (A−D) and fluorescence micrographs (E−G) and relative fluorescence intensity quantification (H) using DyLight 650-functionalized lenticular structures.
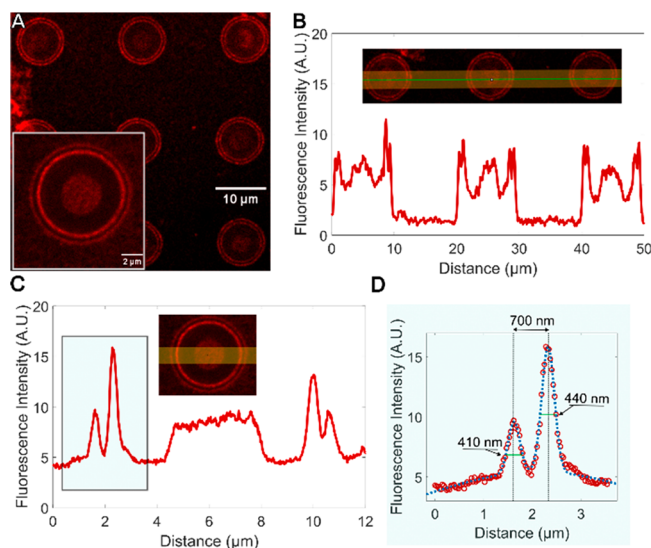

Figure 4. STED microscopy of the ringed fluorescence emission intensity on 10 μm diameter FLIC lenticular substrates by Alexa Fluor 594. The ringed output and plot profiles are shown in (A), the inset with plot profiles in (B) and (C). (D) The Gaussian fit of the intensity profile represents the spatial separation of the elevations of the lenticular domes.

agreement with simulated profiles (using eq 1) as shown in the Supporting Information SI-5 (Figure S4).

When fluorescent dyes are immobilized on the surface of such a structure, bright rings are clearly visible at the circumference of the structure. To illustrate the capacity of fluorescence multiplexing, a more in-depth analysis was made possible by immobilizing several fluorophores, i.e., fluorescein, Cy3, and Cy5, on the surface of lenticular SiO$_2$ structures patterned on Si and observing the ring pattern that formed upon excitation. The corresponding micrographs are presented in Figure 5A. A direct comparison between three fluorescence
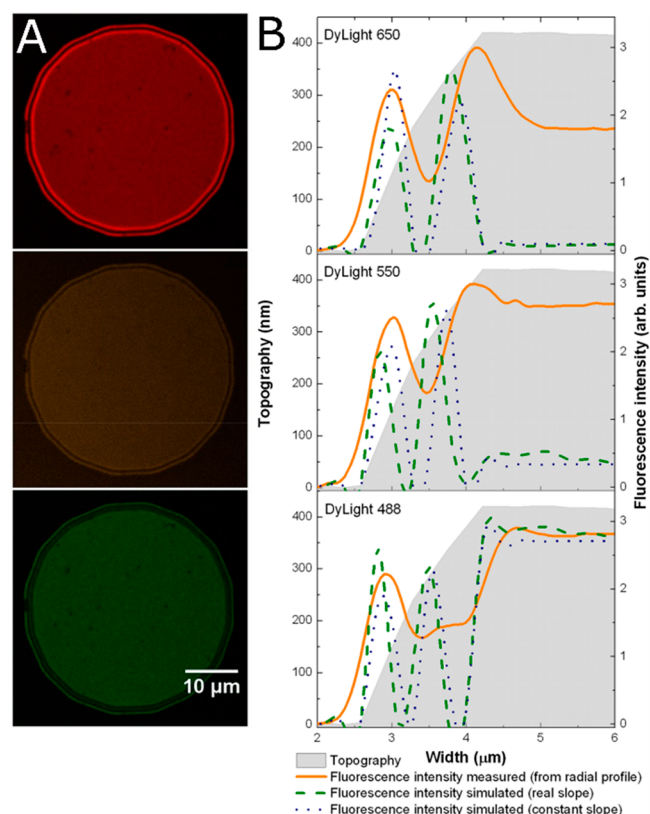

Figure 5. Multiplexing of fluorescence readout on the same lenticular dome substrate. (A) Typical fluorescence micrographs of a 40 μm wide lenticular structure after surface conjugation of DyLight 488, 550, and 650, respectively (bottom to top), accompanied by (B) the corresponding predicted fluorescence intensity plots along a 200 nm long region in space above the two high intensity fluorescence rings. Fluorescence intensity profiles along a cross-section of a lenticular microstructure superimposed on a topographical cross-section (gray filled area). The measured fluorescence intensity was obtained from fluorescence micrographs by radial averaging, while the modeled curves were obtained using the real (imperfect) and artificial (constant slope of the side wall) topography of a lenticular structure.

micrographs (Figure 5A) was done on a qualitative basis only since quantitative comparison requires intensity corrections based on fluorophore quantum yield for nonoptimal excitation and light collection wavelengths (Figure S5). The position of the ring along the side wall was determined by the respective emission wavelength of the fluorophore, while ring brightness is a consequence of electric field intensity along the wall since fluorescence intensity is proportional to the product between the square of the electric field at the excitation and emission wavelengths. This is illustrated in Figure 5B where fluorescence

intensity along a plane spanning 200 nm from the surface of the structure above each of the two rings is plotted. For each fluorophore tested there was at least one position along the side wall of the structure where fluorescence intensity is maximum. The theoretical fluorescence intensity (Figure 5B) was computed as the product between the square of the electric field intensities at the excitation and emission wavelengths of each fluorophore using an iterative procedure described elsewhere.[24,25]

Three approaches were used to infer the fluorescence intensity profile along a cross-section of a lenticular structure (presented in Figure 5): (i) normalized fluorescence intensity profile measured from a lenticular structure; (ii) simulated fluorescence intensity inputting the AFM-measured topography; and (iii) a simulated fluorescence intensity profile using a topography corresponding to a structure with a constant side wall. These profiles were constructed employing the same procedure used to obtain the electric field intensity.

The fluorescence intensity curves in Figure 5B presented a good general agreement between the simulated (dotted green lines) and the measured quantities (orange lines). The lack of perfect overlap can be explained by different facts. First, the measured fluorescence intensity is a radial profile extracted from fluorescence micrographs, whereas the lenticular structures are not perfectly circular but octagonal, thus inducing some distortion manifested through peak widening. Second, the fabrication process, at this point, results in a slightly varying slope. The effect of this difference can be seen by comparing two modeled scenarios, i.e., one using a topographical cross-section from a real lenticular structure and the other relying on an ideal structure with no curvature along the side wall. This curvature will affect the intensity and the width relationship between the two rings. Once corrections are implemented, the simulated behavior approximates considerably better the observed intensity distribution. In addition to that point, when other parameters are considered (fluorescence spectrum, emission filters) the simulated behavior also better accounts for intensity distributions (see SI-6 (Figure S5)), however still not fully covering the experimental value. This is because, most importantly, the 1D model presently used in the simulation is an approximation of the real situation. Not only does this model not account for surface roughness, i.e., nonspecular reflection, but also, high numerical objective effects, e.g., laser depolarization and/or nonplanar wavefront incidence, will strongly influence the fluorescence interference contrast spatial distribution.

The maximization of the electric field at the excitation wavelength in the volume containing the fluorophore is the key common element of fluorescence enhancement on the substrates reported so far in the literature. Additionally, the slides comprising a dielectric stack provide maximum reflectance to recover the light emitted toward the substrate. The simplest approach comprised of a metallic alloy mirror and a SiO_2 spacer will raise problems related to less than perfect intimate contact between the basal and the spacer layers, compared with the perfect $Si-SiO_2$ interface, and therefore an expected loss of fluorescence signal. Alternatively, the lenticular structures can be built with base Si as the reflector, at the cost of intrinsic lower reflectivity. However, this can be alleviated by simply switching to a more effective reflector, with reasonable adhesion to SiO_2, like aluminum. While the architecture reported here exhibits robustness due to well-understood constructive principles and simple design, its

main advantage is the built-in compliance to the fluorescence interference model. Finally, while the fluorescence intensity profile can be predicted with reasonable accuracy for initial designs, further and considerable work is needed to develop 2D and even 3D models, factoring in many qualifications identified above.

Sensitivity Limit of Lenticular FLIC Technology. The experimental validation using protein−protein recognition further demonstrated the analytical capability of FLIC methodology. The receptor-binding domain (RBD) in the spike protein subunit S1 was used as the primary target for vaccines and diagnostics against SARS-CoV-2 (Severe Acute Respiratory Syndrome Coronavirus 2). The dome efficiencies in biorecognition, LoD, and signal-to-noise ratios were compared to terraces in Figure 6 and Figure S6. In Figure
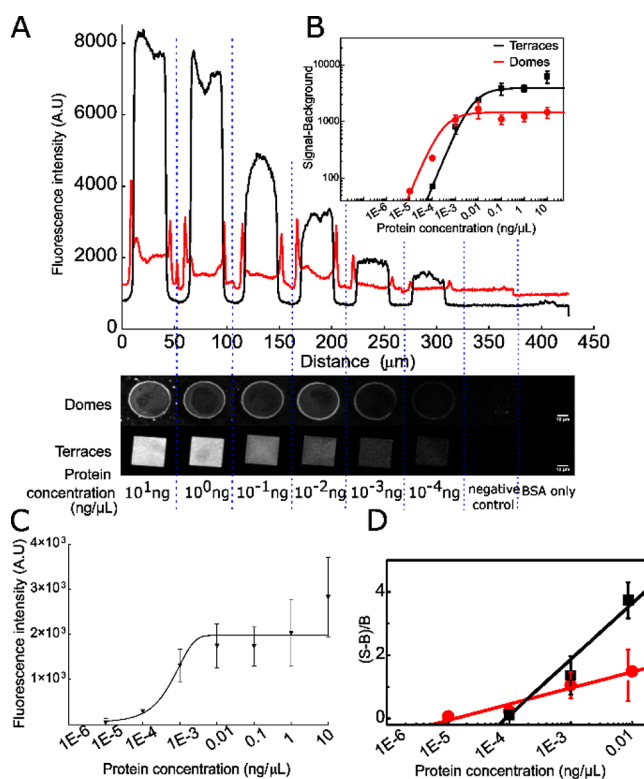

Figure 6. Recognition of the RBD subunit immobilized on 40 μm diameter FLIC-enabled lenticular dome microstructures by an anti-S1 antimouse labeled IgG subunit. (A) Fluorescence intensity plots for the domes (red) and plateaus (black) with the micrographs showing the array of FLIC substrates (below the x-axis). (B) Sensitivity analysis for domes and plateaus in red and black lines, respectively. (C) Graph showing the LoD for the biodetection using dome FLIC substrates ($N = 30$ measurements). (D) $(S - B)/B$ comparison for domes and plateaus in red and black lines, respectively, compares the lower concentrations for both domes and terraces. S, signal; B, background.

S6A and S6B, the average fluorescence intensity readings (dark blue shade) are shown with standard error mean with minima and maxima (lighter blue shade) for more than three plot profiles ($n = 3$). The semitransparent rectangles in the inset (B) show the region used for plotting the profile analysis (C and D). The limit of antigen biorecognition using FLIC-lenticular microstructures is shown in Figure 6A using fluorescence intensity profiles with double fluorescence peaks for domes (red lines) and flat plateaus for terraces (black

lines). The double peaks shown in Figure 6A are the maximum peak intensity comparison at the edges of the lenticular structures for different concentrations. The fluorescence image panel at the bottom of the *x*-axis represents the fluorescence images after biorecognition for domes (top panel) and terraces (bottom panel). The maximum fluorescence intensity reduced drastically for concentrations starting from 0.001 ng/μL. However, different intensity visibility of rings and plateaus was observed for domes and terraces. The definition of FLIC was clear at a high antigen concentration (10 ng/μL RBD-antigen) for domes (FLIC rings) and terraces (FLIC squared substrates). However, the quantitative observation of the least concentration was 10^{-5} ng/μL for domes and 10^{-4} ng/μL for terraces. No detectable fluorescence was observed for negative controls and BSA sample spots. BSA was used as a control to test for nonspecific recognition. These micrographs and plot profiles served as a qualitative observation of the successful recognition of the labeled anti-S1 antibodies on an array of domes or terraces with the surface-functionalized RBD domains.

To quantify the sensitivity and detection limit of FLIC technology, the RBD-S1 antigen concentrations were varied in orders of magnitude, from 1 ng/μL down to 0.00001 ng/μL. Figure 6B (domes - red and terraces - black lines) and Figure 6C (domes only), respectively, present the fluorescence response for these concentrations of the SARS-CoV-2 viral antigen using FLIC substrates, alongside different controls, i.e., BSA, no antigen. For the domes, the detection declined sharply after a concentration of 0.001 ng/μL, although the lenticular concentric rings were still detectable for a concentration of 0.0001 ng/μL (almost no detectable fluorescence was observed for a concentration of 0.00001 ng/μL antigen) (Figure 6B and 6D). Water was used as a negative control, and BSA was used to test the cross-reaction. Unintended binding of the labeled antibodies yielded no detectable fluorescence in both types of the substrate, i.e., domes and terraces. The steepness in the decrease of fluorescence intensity was prominent for terraces compared to domes, measured quantitatively by using signal/noise ratios (Figure 6B and 6D) and qualitatively by using surface plots (Figure S6D), suggesting that the FLIC-lenticular substrates can be effectively used for sensitive diagnostic applications. The FLIC lenticular structures detected antigens at concentrations as low as 0.001 ng/μL to 0.0001 ng/μL, while a review[42] of the present commercial ELISA-based lateral flow SARS-CoV2 point of care assays reported detection limits ranging between 0.01 ng/μL and 0.005 ng/μL. While the example used here is relevant to a diagnostically important target, i.e., RBD of the SARS-CoV2, the methodology can be reasonably extended for DNA, RNA, and other complementary interactions.

CONCLUSIONS

This work describes two types of microstructured surfaces designed to modulate, by optical interference, the spatial distribution of a fluorescence signal, with the confinement principle illustrated by conjugating a fluorophore to the surface. SiO$_2$ microterraces were patterned on Si- and on Pt-covered substrates with varying heights to maximize the fluorescence emission and these structures were used to calibrate the designs of SiO$_2$-on-Si microstructured domes, which offer the important advantage of obtaining an optimal FLIC response irrespective of the wavelengths of the fluorophores used. The FLIC lenticular structures were further

characterized in terms of spatial resolution when the specific FLIC rings can be resolved at distances around 700 nm. Finally, the detection sensitivity of FLIC technology was tested on a contemporary relevant application, i.e., recognition of the RBD subunit of SARS-Cov2 by anti-S1 antimouse. The self-optimization of the amplified fluorescence signals by FLIC lenticular structures suggests that this technology can be used for a large variety of diagnostics applications.

■ ASSOCIATED CONTENT

ⓢ Supporting Information

The Supporting Information is available free of charge at https://pubs.acs.org/doi/10.1021/acssensors.2c01939.

> Brief description of contents. Table S1. Imaging parameters used for the FLIC 1D model. Table S2. Calculation of reflectivity coefficients and data fitting. Figure S1. Diagram showing a simplified optical setup valid for the substrates presented in this paper. Direct excitation and emission light, respectively, interfere with their reflected counterparts, creating standing waves. Figure S2. Experimental data fitted with Equation SI.5 (left: Si reflector, right: Pt reflector). Table S3. Quality of fit values. Table S4. ToF-SIMS relative ion abundance. Figure S3. Effect of optical slicing on contrast (A and B); fluorescence signal on an array of lenticular structures, without SiO$_2$ base (C) and with a 60 nm SiO$_2$ intermediate layer (D). Figure S4. Comparison of the simulated and experimental fluorescence intensity readout using STED imaging analysis. Figure S5. Simulation of the fluorescence output for multiplex imaging. Figure S6. Recognition and comparison of fluorescence output between terraces and domes (PDF)

■ AUTHOR INFORMATION

Corresponding Authors

Cyril Favard − *Membrane Domains and Viral Assembly, Montpellier Infectious Disease Research Institute, CNRS UMR9004, 34293 Cedex Montpellier, France;* Email: cyril.favard@irim.cnrs.fr

Dan V. Nicolau − *Department of Electrical Engineering & Electronics, University of Liverpool, Liverpool L69 3GJ, U.K.; Department of Bioengineering, McGill University, Montreal H3A 0C3, Canada;* ⓞ orcid.org/0000-0002-9956-0600; Email: dan.nicolau@mcgill.ca

Authors

Serban Dobroiu − *Department of Electrical Engineering & Electronics, University of Liverpool, Liverpool L69 3GJ, U.K.; Department of Bioengineering, McGill University, Montreal H3A 0C3, Canada*

Falco C.M.J.M. van Delft − *MiPlaza, Philips Research Europe, 5656 AE Eindhoven, The Netherlands; Molecular Sense Ltd., Liverpool L36 8HT, U.K.;* ⓞ orcid.org/0000-0002-3234-2211

Ayyappasamy Sudalaiyadum Perumal − *Department of Bioengineering, McGill University, Montreal H3A 0C3, Canada*

Shantoshini Dash − *Department of Bioengineering, McGill University, Montreal H3A 0C3, Canada*

Jenny Aveyard − *Department of Electrical Engineering & Electronics, University of Liverpool, Liverpool L69 3GJ, U.K.*

Jeroen van Zijl − *MiPlaza, Philips Research Europe, 5656 AE Eindhoven, The Netherlands*

Jaap Snijder − *MiPlaza, Philips Research Europe, 5656 AE Eindhoven, The Netherlands*

Eric van den Heuvel − *MiPlaza, Philips Research Europe, 5656 AE Eindhoven, The Netherlands*

Jurgen van Berkum − *MiPlaza, Philips Research Europe, 5656 AE Eindhoven, The Netherlands*

Marie Pierre Blanchard − *Montpellier Ressources Imagerie, BioCampus, University of Montpellier, CNRS, INSERM, 34000 Montpellier Cedex, France*

Complete contact information is available at:
https://pubs.acs.org/10.1021/acssensors.2c01939

Author Contributions

Funding

Notes

The authors declare no competing financial interest.

■ ACKNOWLEDGMENTS

■ REFERENCES

(1) Noel, D. D.; Olefongo, D.; N'Goran Etienne, L.; Ali, K.; Désiré, L. H.; Giacomelli, M.; Pinelli, M.; Joseph, D. A.; Malerba, G.; Delledonne, M. Interaction between microarray design strategies and data pre-processing procedures in gene expression differential analysis: A computational statistical survey. *Research Journal of Biotechnology* 2020, 15 (12), 69−86.

(2) Sarwat, M.; Yamdagni, M. M. DNA barcoding, microarrays and next generation sequencing: Recent tools for genetic diversity estimation and authentication of medicinal plants. *Critical Reviews in Biotechnology* 2016, 36 (2), 191−203.

(3) Diehl, F.; Grahlmann, S.; Beier, M.; Hoheisel, J. D. Manufacturing DNA microarrays of high spot homogeneity and reduced background signal. *Nucleic Acids Res.* 2001, 29 (7), 38e−38.

(4) Moore, C. D.; Ajala, O. Z.; Zhu, H. Applications in high-content functional protein microarrays. *Curr. Opin. Chem. Biol.* 2016, 30, 21−27.

(5) Rasnik, I.; McKinney, S. A.; Ha, T. Nonblinking and long-lasting single-molecule fluorescence imaging. *Nat. Methods* 2006, 3 (11), 891−893.

(6) Becker, W. Fluorescence lifetime imaging - techniques and applications. *J. Microsc.* 2012, 247 (2), 119−136.

(7) Demchenko, A. P. Photobleaching of organic fluorophores: Quantitative characterization, mechanisms, protection. *Methods and Applications in Fluorescence* 2020, 8 (2), 022001.

(8) Lee, K. B.; Kim, J. S.; Cho, J. B.; Park, B. G.; Lee, W.; Oh, M. K. Size-controllable quartz nanostructure for signal enhancement of DNA chip. *Biosens Bioelectron* 2011, 26 (5), 2085−2089.

(9) Liu, W. T.; Murthy, B. R.; Ng, J. K. K.; Selamat, E. S.; Balasubramanian, N. Silicon nanopillar substrates for enhancing signal intensity in DNA microarrays. *Biosens Bioelectron* 2008, 24 (4), 723−728.

(10) Liu, J. H.; Gu, C. P.; Huang, J. R.; Ni, N.; Li, M. Q. Detection of DNA hybridization based on SnO(2) nanomaterial enhanced fluorescence. *J. Phys. D Appl. Phys.* 2008, 41 (17), 175103.

(11) Lu, C.; Lipson, R. H. Interference lithography: a powerful tool for fabricating periodic structures. *Laser Photonics Rev.* 2010, 4 (4), 568−580.

(12) Ivanova, E. P.; Wright, J. P.; Pham, D.; Filipponi, L.; Viezzoli, A.; Nicolau, D. V. Polymer microstructures fabricated via laser ablation used for multianalyte protein microassay. *Langmuir* 2002, 18 (24), 9539−9546.

(13) Nicolau, D. V.; Ivanova, E. P.; Fulga, F.; Filipponi, L.; Viezzoli, A.; Dobroiu, S.; Alekseeva, Y. V.; Pham, D. K. Protein immobilisation on micro/nanostructures fabricated by laser microablation. *Biosens Bioelectron* 2010, 26 (4), 1337−1345.

(14) Deng, X.; He, S.; Xie, F.; Friedmann, C.; Hess, H.; Lahann, J. Ultrasensitive in Situ Fluorescence Analysis using Modulated Fluorescence Interference Contrast at Nanostructured Polymer Surfaces. *Adv. Mater.* 2016, 28 (12), 2367−2373.

(15) Aveyard, J.; Hedegaard, T.; Bilenberg, B.; Nicolau, D. V. Microfabricated magnetic bead polydimethylsiloxane microarrays. *Microelectron. Eng.* 2010, 87 (5−8), 760−764.

(16) Filipponi, L.; Sawant, P. D.; Fulga, F.; Nicolau, D. V. Microbeads on microposts: An inverted architecture for bead microarrays. *Biosens Bioelectron* 2009, 24 (7), 1850−1857.

(17) Lin, D. M.; Moran-Mirabal, J. M.; Tan, C. P.; Orth, R. N.; Williams, E. O.; Craighead, H. G. Controlling microarray spot morphology with polymer liftoff arrays. *Anal. Chem.* 2007, 79 (3), 1109−1114.

(18) Brandstatter, M.; Fromherz, P.; Offenhausser, A. Fluorescent Dye Monolayers on Oxidized Silicon. *Thin Solid Films* 1988, 160 (1−2), 341−346.

(19) Lambacher, A.; Fromherz, P. Fluorescence interference-contrast microscopy on oxidized silicon using a monomolecular dye layer. *Appl. Phys. a-Mater.* 1996, 63 (3), 207−216.

(20) Parthasarathy, R.; Groves, J. T. Optical techniques for imaging membrane topography. *Cell Biochem Biophys* 2004, 41 (3), 391−414.

(21) Conzone, S. D.; Redkar, R. J. Reproducible, low cost arraying achieved with a multiplexed approach. *EBR - European Biopharmaceutical Review* 2004, 52−55.

(22) Redkar, R. J.; Schultz, N.; Scheumann, V.; Burzio, L. A.; Haines, D. E.; Metwalli, E.; Becker, O.; Conzone, S. D. Signal and Sensitivity Enhancement Through Optical Interference Coating for DNA and Protein Microarray Applications. *Journal of Biomolecular Technology* 2006, 17 (2), 122.

(23) Schultz, N.; Conzone, S. D.; Becker, O.; Haines, D.; Pawlowski, E.; Scheumann, V. Arrangement for fluorescence amplification. USA US7939339, 2011.

(24) Dobroiu, S.; van Delft, F. C. M. J. M.; Aveyard-Hanson, J.; Shetty, P.; Nicolau, D. V. Fluorescence Interference Contrast-enabled structures improve the microarrays performance. *Biosens. Bioelectron.* 2019, 123, 251−259.

(25) Bartolini, M.; Naldi, M.; Nicolau, D. V.; van Delft, F. C. M. J. M.; Van Zijl, J.; Snijder, J.; van den Heuvel, E. F. C.; Naburgh, E. P.; Calonghi, N.; Andrisano, V. Fluorescence biosensing micropatterned surfaces based on immobilized human acetylcholinesterase. *Anal. Bioanal. Chem.* 2013, 405 (2−3), 795−804.

(26) Horcas, I.; Fernandez, R.; Gomez-Rodriguez, J. M.; Colchero, J.; Gomez-Herrero, J.; Baro, A. M. WSXM: A software for scanning probe microscopy and a tool for nanotechnology. *Rev. Sci. Instrum.* 2007, 78 (1), 013705.

(27) Rasband, W. S. *Image J*. 1997−2011. (http://rsbweb.nih.gov/ij/) (accessed).

(28) De Man, B.; Basu, S.; Chandra, N.; Dunham, B.; Edic, P.; Iatrou, M.; McOlash, S.; Sainath, P.; Shaughnessy, C.; Tower, B. CatSim: a new computer assisted tomography simulation environment. In *Medical Imaging 2007: Physics of Medical Imaging*; SPIE, 2007; Vol. *6510*, pp 856−863.

(29) Farnós, O.; Venereo-Sánchez, A.; Xu, X.; Chan, C.; Dash, S.; Chaabane, H.; Sauvageau, J.; Brahimi, F.; Saragovi, U.; Leclerc, D. Rapid High-Yield Production of Functional SARS-CoV-2 Receptor Binding Domain by Viral and Non-Viral Transient Expression for Pre-Clinical Evaluation. *Vaccines (Basel)* **2020**, *8* (4), 654.

(30) Dangui, V.; Digonnet, M. J. F.; Kino, G. S. Determination of the mode reflection coefficient in air-core photonic bandgap fibers. *Opt. Express* **2007**, *15* (9), 5342−5359.

(31) Hecht, E.; Zajac, A.; Zajac, A. *Optics*; Addison-Wesley Publishing Company, 1987.

(32) Yuk, J. S.; MacCraith, B. D.; McDonagh, C. Signal enhancement of surface plasmon-coupled emission (SPCE) with the evanescent field of surface plasmons on a bimetallic paraboloid biochip. *Biosens. Bioelectron.* **2011**, *26* (7), 3213−3218.

(33) Halpern, A. R.; Chen, Y.; Corn, R. M.; Kim, D. Surface plasmon resonance phase imaging measurements of patterned monolayers and DNA adsorption onto microarrays. *Anal. Chem.* **2011**, *83* (7), 2801−2806.

(34) Volle, J. N.; Chambon, G.; Sayah, A.; Reymond, C.; Fasel, N.; Gijs, M. A. M. Enhanced sensitivity detection of protein immobilization by fluorescent interference on oxidized silicon. *Biosens Bioelectron* **2003**, *19* (5), 457−464.

(35) Choumane, H.; Ha, N.; Nelep, C.; Chardon, A.; Reymond, G. O.; Goutel, C.; Cerovic, G.; Vallet, F.; Weisbuch, C.; Benisty, H. Double interference fluorescence enhancement from reflective slides: Application to bicolor microarrays. *Appl. Phys. Lett.* **2005**, *87* (3), 031102.

(36) Marino, V.; Galati, C.; Arnone, C. Optimization of fluorescence enhancement for silicon-based microarrays. *Journal of biomedical optics* **2008**, *13* (5), 054060.

(37) Cretich, M.; di Carlo, G.; Longhi, R.; Gotti, C.; Spinella, N.; Coffa, S.; Galati, C.; Renna, L.; Chiari, M. High Sensitivity Protein Assays on Microarray Silicon Slides. *Anal. Chem.* **2009**, *81* (13), 5197−5203.

(38) Rancourt, J. D. *Optical thin films: user handbook*; SPIE Optical Engineering Press, 1996.

(39) Cook, C. Q.; Amir, A. Theory of chirped photonic crystals in biological broadband reflectors. *Optica* **2016**, *3* (12), 1436−1439.

(40) Hell, S. W.; Wichmann, J. Breaking the diffraction resolution limit by stimulated emission: stimulated-emission-depletion fluorescence microscopy. *Optics letters* **1994**, *19* (11), 780−782.

(41) Klar, T. A.; Hell, S. W. Subdiffraction resolution in far-field fluorescence microscopy. *Optics letters* **1999**, *24* (14), 954−956.

(42) Corman, V. M.; Haage, V. C.; Bleicker, T.; Schmidt, M. L.; Mühlemann, B.; Zuchowski, M.; Jo, W. K.; Tscheak, P.; Möncke-Buchner, E.; Müller, M. A.; et al. Comparison of seven commercial SARS-CoV-2 rapid point-of-care antigen tests: a single-centre laboratory evaluation study. *Lancet Microbe* **2021**, *2* (7), No. 311.

📖 Recommended by ACS